Non-aqueous synthesis of homogeneous molybdenum silicate microspheres and their application as heterogeneous catalysts in olefin epoxidation and selective aniline oxidation

Non-aqueous synthesis of homogeneous molybdenum silicate microspheres and their application as heterogeneous catalysts in olefin epoxidation and selective aniline oxidation

David Skoda[a,*], Barbora Hanulikova[a], Ales Styskalik[b], Vit Vykoukal[b,c], Petr Machac[b], Pavel Urbanek[a], Eva Domincova Bergerova[a], Lucie Simonikova[b], Ivo Kuritka[a]

[a]*Centre of Polymer Systems, Tomas Bata University in Zlin, tr. Tomase Bati 5678, Zlin, CZ 76001, Czech Republic*

[b]*Department of Chemistry, Faculty of Science, Masaryk University, Kotlarska 2, Brno, CZ6H37, Czech Republic*

[c]*Central European Institute of Technology, Masaryk University, Kamenice 5, Brno, CZ 62500, Czech Republic*

[*]*Corresponding author: E-mail address: dskoda@utb.cz (D. Skoda).*

ABSTRACT

In this work, a novel synthesis of homogeneous molybdenum silicate spheres under non-aqueous conditions is presented. A preparation method is based on the condensation of molybdenum metal-organic framework-based precursor solution prepared via a microwave-assisted approach from bis(acetylaceto nato)dioxomolybdenum and biphenyl-4,4'-dicarboxylic acid with 3-aminopropyltriethoxysilane under non-aqueous conditions. The as-prepared product was calcined at 500 °C to obtain amorphous and porous molybdenum silicate microspheres with homogeneously distributed molybdenum species within silicate matrix. The microspheres exhibit an average size of about 480 nm. This material was further studied as a heterogeneous catalyst for the epoxidation of olefins via the model catalytic epoxidation of cyclohexene with cumylhydroperoxide. High catalytic activity at the moderate temperature (65 °C) with the conversion of 86% after 2 h and the high selectivity to cyclohexene oxide has been achieved. In addition, molybdenum silicate microspheres exhibit catalytic activity and high selectivity in the oxidation of aniline to nitrosobenzene.

Keywords: Molybdenum silicate, non-aqueous, microspheres, catalyst, epoxidation, aniline oxidation

Introduction

In recent years, an increasing effort of researchers has been devoted to the development of environmentally friendly processes in industrial and materials chemistry. In this regard, the use of novel and advanced heterogeneous reusable catalysts, which can be easily separated from the reaction mixture, has been of great interest as they can contribute to the waste minimization and facilitation of industrial processes. Furthermore, from the environmental point of view, that reduce undesired byproducts, safer oxidizing reagents, less hazardous waste, and low energy input are highly desired [**1**].

Heterogeneous catalysts containing transition metal-based active sites, for example, Ti, Zr, Sn, W, and Mo, have shown enormous potential in various catalytic reactions such as epoxidation, olefin metathesis, epoxide ring-opening reactions, and oxidation of amines [**1**]. The epoxidation of olefins has gained immense attention in both academic and industrial research fields. Epoxides are highly versatile intermediates and valuable compounds produced on an industrial scale [**2**]. Further, a ring-opening reaction of the epoxides provides a wide range of chemicals, such as pharmaceuticals, detergents, paints, agrochemicals, polymers, surfactants, corrosion protection agents, lubricating oils, food additives, cosmetics, etc. On an industrial scale, the epoxides are produced using peracids, which leads to a release of toxic and corrosive wastes [**3**]. Oxidation of amines to nitroso- compounds is another important functional transformation in the organic synthesis [**4,5**]. The aromatic nitroso-compounds are extensively used as chemical precursors for a wide range of valuable materials such as dyes, pharmaceuticals, perfumes, and plastics [**6**].

The catalytic activity of transition metal-based catalysts is assigned to their Lewis and/or Brensted acidity **[2,7,8]**. High activity and selectivity of molybdenum, tungsten, vanadium, and titanium silicate-based catalysts in olefin epoxidation have been demonstrated when using hydroperoxides (e.g., tert-butyl hydroperoxide (TBHP) and H_2O_2) as oxidizing agents [**7,9,10**]. Moreover, the advantages of Mo compounds such as low cost, availability, environmental friendliness, and non-toxicity are getting closer to meet the green principles [**2,11,12**].

During ongoing research, a wide range of supports, including silica [**13-15**], silica-alumina [**16,17**], zeolites [**18**], metal-organic frameworks [**19**], and carbon [**20**] have been reported. To improve the properties of catalysts, such as stability and recyclability, an immobilization of active species on the support has been established as an effective approach. Conventional methods for supported catalyst preparation such as impregnation, thermal spreading, and grafting usually involve a two-step procedure. Unfortunately, these strategies suffer from several limitations such as the inhomogeneous distribution of the active species on (over) the support (e.g., not deposited inside the pores of the support [**21**]), the formation of inactive species, or the lack of interaction between the active species and the support resulting in the leaching of active sites from the catalyst [**22,23**]. The impregnation methods can be improved, for example, by changing the molybdenum precursor nature or increasing the molybdenum content in the dispersion [**24**]. Masteri-Farahani et al. have modified MCM-41 surface and anchored bis(acetylacetonato)dioxomolybdenum(VI) complex as an active species of catalyst [**26**]. Farook et al. have described rice husk-derived silica-supported amorphous molybdenum catalysts prepared via the sol-gel method [**27**]. The acid-catalyzed sol-gel synthesis of MoO_3-SiO_2 composite epoxidation catalyst using Mo(V)-isopropoxide precursor has been reported by Arnold et al. [**25**]. However, the presented catalyst exhibited significant leaching of the active Mo species after successive catalytic cycles.

Further, the involvement of morphology-controlled silica incor-porating/embedding molybdenum oxide nanoparticles (NPs) have been developed; for example, monodispersed SiO_2 spheres embedding MoO_3 nanoparticles prepared with Brij-58/cyclohexane/water reverse micro-emulsions have been presented by Wang et al. [**28**]. Spherical MoO_3@SiO_2 nanoreactors prepared via impregnation of hollow mesoporous silica spheres (HMSS) and rose-like molybdenum incorporated silica nanoparticles have been recently reported by Shen et al. [**29,30**]. Recent work by Gu et al. has demonstrated MoO_3 nanoparticles in 3D dendritic mesoporous silica nanospheres [**31**]. Kuwahara et al. have reported a one-pot synthesis of hollow silica spheres with encapsulated molybdenum oxide [**9**]. A highly dispersed molybdenum incorporated hollow mesoporous silica spheres prepared via a two-step process have been demonstrated by Shen et al. [**15**]. Finally, Mo-containing hierarchical macro-mesoporous SBA-15 catalyst for olefin epoxidation has been prepared via dual-templating technique by Zhang et al. [**32**].

Following the survey given above, it can be stated that rapid and one-step syntheses of stable and reusable catalysts featuring homogeneous Mo distribution, high activity, and selectivity at moderate temperatures are still challenging issues. A low amount of catalyst required for the reaction is another appreciated advantage.

As it has been reported previously, non-aqueous sol-gel methods were found as efficient pathways for the preparation of homogeneous and mesoporous metallosilicate catalysts with Lewis acidity [**7,33-35**]. It is worth mentioning that avoiding the hydrolysis step within the non-aqueous sol-gel process leads to a higher degree of condensation, deeper crosslinking, and thus better homogeneity. Phase separation of oxides, which is usually caused by hydrolysis of precursors followed by M-OH species formation, is prevented [**35**].

Herein, we introduce a novel, fast, and simple non-aqueous approach for homogeneous molybdenum silicate microspheres preparation. The synthesis is based on a microwave-assisted preparation of molybdenum metal-organic framework (Mo-Bpdc) solution serving as molybdenum precursor that is subsequently mixed with 3-aminopropyltriethoxysilane (APTES), result- ing in precipitation of microspheres (Mo-Bpdc-APTES). In contrast to conventional impregnation methods, there is no need to prepare silica support separately in the presented non-aqueous method. Instead, the homogeneous molybdenum silicate material is obtained within one-step condensation. Utilization of biphenyl-4, 4'-dicarboxylic acid linker was found to improve condensation between Mo-Bpdc MOF precursor and APTES. After the annealing of as-prepared spheres, porous and amorphous molybdenum silicate spheres with homogeneous Mo distribution are obtained. It was demonstrated that described process enables high loading of molybdenum without the MoO_3 phase separation. Molybdenum silicate microspheres were used as heterogeneous catalysts for the epoxidation of cyclohexene. High conversion and selectivity to cyclohexene oxide were observed. Molybdenum silicate microspheres also exhibited appreciable catalytic activity and high selectivity in the oxidation of aniline to nitrosobenzene.

Experimental

Chemicals

Bis(acetylacetonato)dioxomolybdenum(VI) ($MoO_2(Acac)_2$, 99%, M_w = 326.15 g mol^{-1}), biphenyl-4,4'-dicarboxylic acid (H_2Bpdc, M_w = 242.23 g mol^{-1}, 97%), (3-aminopropyl)triethoxysilane ($H_2N(CH_2)_3Si(OC_2H_5)_3$, APTES, M_w = 221.37, 98%), cyclohexene (M_w = 82.14 g mol^{-1}, 99%), cumene hydroperoxide (CmOOH, M_w = 152.19 g mol^{-1}, technical grade 80%), cyclohexene oxide (98%), and nitrosobenzene (NOB, Mw = 107.11 g mol^{-1}, 97%) were supplied from Sigma Aldrich. N,N'-dimethylformamide (DMF, p.a.), toluene (p.a.) and aniline (p.a.) were purchased from Merck.

Synthesis of Mo-Bpdc-APTES

At first, Mo-Bpdc precursor solution was prepared in a microwave reactor. The $MoO_2(acac)_2$ (0.3264 g, 1.00 mmol) was dissolved in 50 cm^3 of DMF in a Teflon container. After the dissolution of the molybdenum precursor, H_2Bpdc (0.2422 g, 1.00 mmol) was added and the container was closed tightly and placed into a microwave reactor. Microwave power was set to 50% (300 W) and the reaction mixture was heated up to 160 °C under microwave irradiation for 30 min. The microwave-assisted reaction record is given in **supplementary information (Fig. 1S)**. Once the reaction mixture was cooled down to room temperature, the yellow-orange transparent solution of Mo-Bpdc precursor (**Fig. 2S**)

was slowly dropped into a stirred solution of APTES (1.1168 g, 5.045 mmol) in 50 cm^3 DMF. During the mixing, the reaction mixture began to cloudy and a white precipitate was formed. Once the whole volume of Mo-Bpdc precursor was added into APTES solution, the reaction was stirred at room temperature for 4 hours. Then, the precipitate was separated by centrifugation at 6000 rpm, washed with DMF, and dried in an oven at 90 °C overnight. The yield of Mo-Bpdc-APTES was 0.728 g.

The analysis of Mo-Bpdc-APTES powder product:

FTIR (ATR, diamond crystal, cm^{-1}) ν: 474 m, 537 w (δ CC, bending), 674 m (ring out-of-plane), 702 w, 773 s (ring out-of-plane), 766 s (δ CH, bending), 799 v, 832 m (δ CH), 859 w (δ CH), 914 w (δ CH, bending), 961 w, 1003 s (ν), 1062 s (ν Si-O-Si), 1092 s (ν Si-O-Si), 1226 vw (ν CC), 1260 vw (ν Si-C), 1371 vs (ν_{sym} COO), 1439 vw (ν_{sym} COO), 1525 m (ν_{asym} COO), 1578 m (ν_{asym} COO), 1604 w, 1660 m (ν C = O), 2863 vw, 2928 vw (ν CH_3).

Elemental analysis

ICP OES: 4.8 ± 0.1 wt% Mo, 9.97 ± 0.04 wt% Si.

C,H,N flash: 43.19 wt% C, 7.30 wt% N, 5.98 wt% H.

MAS NMR (Mo-Bpdc-APTES): ^{13}C TOSS CPMAS δ; ppm: 13.2 (-**C**$H_2CH_2CH_2NH_2$), 24.3 (-CH_2**C**$H_2CH_2NH_2$), 33.2 (-N**C**H_3), 38.7 (-N**C**H_3), 45.0 (-CH_2CH_2**C**H_2NH_2), 60.4 (CH_3**C**H_2O-), 128.6 (**C**H -aromatic), 139.3 (**C**H -aromatic), 164.0 (CH_3**C**(O) - monodentate), 176.1 (CH_3**C**(O) - bidentate); ^{29}Si CPMAS δ; ppm: -51.4, -60.0, -66.6.

Calcination of Mo-Bpdc-APTES (MoSi-500)

The calcination process of the Mo-Bpdc-APTES product was carried out in a Nabertherm LE 4/11/R6 tubular furnace under an atmosphere of the air at the temperature of 500 °C for 3 hours. The heating was set up to 500 °C with a rate of 5 °C min^{-1}. The calcined sample was labeled as MoSi-500.

Epoxidation of cyclohexene

Catalytic properties of the molybdenum silicate spheres (MoSi-500) obtained from Mo-Bpdc-APTES were tested in a model epox-idation of cyclohexene with CmOOH following the reported procedures [**10,36**]. The catalyst (20 mg) was added to a vial flask. Toluene (5 cm^3) and cyclohexene (2.5 cm^3, 24.7 mmol) were added, and the temperature of the reaction mixture was increased to 65 °C. Then, CmOOH (0.92 cm^3, 4.9 mmol) was added to the stirred solution. The initial cyclohexene:CmOOH molar ratio for epox-idation reaction in 5:1. After 2 hours, the reaction was stopped and the reaction products were analyzed by ^{1}H NMR spectroscopy and GC-MS spectrometry. On the one hand, GC-MS conversion determination was done with the use of a calibration curve of known contents of cyclohexene oxide and CmOOH; conversion was based on CmOOH. On the other hand, ^{1}H NMR conversion determination was based on cyclohexene. To confirm that no active sites are leached from the catalyst, the leaching test was performed as follows: 25 mg of catalyst was refluxed in 10 cm^3 of toluene at 120 °C for 4 h. Then, the catalyst was separated by centrifugation. After the separation of the catalyst, cyclohexene (2.5 cm^3, 24.7 mmol) and CmOOH (0.92 cm^3, 4.9 mmol) were added into the solution and this reaction mixture was tested in an epoxidation reaction for 2 hours at 65 °C. After the reaction, the reaction mixture was analyzed by GC-MS. A blank reaction without the catalyst was performed at the same

conditions as described above. The TOF (turn-over frequency) number was calculated as follows: TOF [h^{-1}] = number of moles of reactant consumed/(mole of Mo in catalyst * time) [**37,38**].

Oxidation of aniline

Catalytic properties of the MoSi-500 catalyst were tested in the model oxidation of aniline with CmOOH at room temperature. The catalyst (20 mg) was added to a vial flask. Toluene (10 cm^3) and aniline (0.456 cm^3, 4.9 mmol) were added. Then, CmOOH (0.920 cm^3, 4.9 mmol) was added to the stirred solution. The reaction products were analyzed by GC-MS after 2 h, 4 h, and 24 h. A blank reaction without the catalyst was performed as well. Determination of conversion was done using a calibration curve of known contents of aniline and NOB.

Characterization techniques

Microwave-assisted procedure

The Mo-Bpdc precursor solution was synthesized under an ambient atmosphere in a PTFE-lined microwave reactor ERTEC Magnum II (600 W; 2.45 GHz). Microwave power was set to 50% (300 W) and the reaction mixture was heated up to 160 °C. The reaction duration was 30 min. The product separation was performed on a Heraeus Multifuge X3R centrifuge by Thermo Scientific at 6000 rpm for 5 min.

Chemical/elemental analyses

The GC-MS measurement of reaction byproducts was performed on an ISQ Series single quadrupole mass spectrometer coupled with a Trace 1300 gas chromatograph. The gas chromatograph was equipped with a Rxi-5 ms column (30 m, 0.25 mm, film thickness 0.25 μm) and the temperature program was used as follows: 80-240 °C with the ramp 10 °C min^{-1}, held at 240 °C for 1 min. Split injection mode (60 ml min^{-1}, split ratio 60) was set with the inlet and transfer line temperature of 280 °C, and EI source 220 °C (ionization energy: 70 eV, emission current: 30 μA). Molybdenum and silicon content in the prepared materials was determined by ICP-OES spectroscopy performed on an iCAP 6500 spectrometer (molybdenum spectral line λ = 202.030 nm, silicon spectral line λ = 250.690 nm). The elemental composition analysis was conducted with Flash 2000 CHNS/O + MAS200R. All instruments are part of Thermo Scientific portfolio.

XRD diffraction analysis

The powder XRD patterns were recorded on a Rigaku MiniFlex 600 diffractometer equipped with a CoKα (λ = 1.7903 Å) X-ray tube (40 kV, 15 mA). Data processing was done with Rigaku PDXL2 software.

Infrared, Raman, and DRUV/Vis spectroscopy

The FTIR spectra were recorded on a Thermo Nicolet 6700 spectrometer using an ATR technique with the diamond crystal (resolution 2 cm^{-1}, 4000-400 cm^{-1}). Raman spectroscopy was performed on a Thermo Raman microscope Nicolet DXR equipped with a He-Ne laser with excitation wavelength 633 nm (power 1 and 4 mW). The spectra were recorded from 2000 to 50 cm^{-1}. The DRUV/Vis measurement was carried out on a UV-Vis spectrometer Avantes Avaspec 2048 with an integration sphere with a 50 mm diameter and an integration time of detector 1000 ms. Pyridine adsorption test was performed as follows: 30 mg of calcined product was placed into a beaker (5 cm^3 volume) and tightly closed in a Duran bottle (100 cm^3 volume) containing 2 cm^3 of pyridine. Pyridine adsorption took 2 h and then the powder product was dried in a vacuum oven at 150 °C for 1 h. Adsorbed pyridine was identified by FTIR spectroscopy.

X-ray photoelectron spectroscopy

X-ray photoelectron spectroscopy measurements were carried out on a Kratos Analytical Axis Supra spectrometer equipped with monochromatized Al-Kα radiation (1486 eV). The sample powders, pressed in small stainless troughs of 4 mm diameter, were placed on an insulating homemade ceramic carousel. The pressure in the analysis chamber was around 10^{-6} Pa. The analyzed area was approximately 1.4 mm^2 and the pass energy was set at 150 eV. The C 1s peak of carbon has been fixed to 284.8 eV to set the binding energy scale [**39**]. Data treatment was performed with the CasaXPS program (Casa Software Ltd, UK) and some spectra were deconvoluted with the least-squares fitting routine provided by the software with a Gaussian/Lorentzian (85/15) product function after subtraction of a nonlinear baseline.

Thermal analysis and heat treatment

Thermogravimetric analyses were performed on a Setaram LabSys Evo instrument with TG/DSC sensor in an atmosphere of the air (heating ramp 5 °C min^{-1}, up to 1000 °C, airflow 60 cm^3 min^{-1}) and helium (5 °C min^{-1}, up to 900 °C, 60 ml min^{-1}). Dried powders were heated in a Nabertherm LE 4/11/R6 tubular furnace at 500 °C (5 °C min^{-1}) for 3 hours in the air atmosphere.

Microscopy

The scanning electron microscopy (SEM) was obtained with Nova NanoSEM (FEI) operated at 5 kV and equipped with a Schot- tky field emission gun (FEG) electron source and TLD secondary-electron detector. The SEM energy dispersive X-ray (EDX) analysis was performed with EDX spectrometer Octane Plus (EDAX, AME-TEK, Inc) with an SDD detector. The transmission electron microscopy was performed with a high-resolution TEM (HRTEM) Titan Themis 60-300 High Base (Thermo Fisher Scientific) operated at 300 kV and equipped with a high-brightness X-FEG electron source and a spherical aberration image (Cs)-corrector. The scanning TEM EDX (STEM-EDX) analysis was performed with a Super-X spectrometer (Thermo Fisher Scientific) with four 30 mm^2 windowless detectors. The STEM imaging was performed with a high-angular annular dark-field (HAADF) detector (Fishione) providing atomic Z-contrast. The sample for TEM was dispersed in methanol and 4 µl of this suspension was placed on a QuantiFoil R 2/1 300 mesh copper grid and allowed to dry by evaporation at ambient temperature.

Nitrogen adsorption/desorption

Nitrogen adsorption/desorption isotherms were collected at the temperature of 77 K on BELsorp Mini II (Japan). Before measurement, the samples were degassed in the BELsorp preparation unit at 100 °C for 19 hours. Surface areas (SA) and total pore volumes (V_{tot} at p/p_0 = 0.99) were determined by volumetric techniques [**40,41**]. The specific surface area was calculated from the multipoint Brunauer-Emmet-Teller (BET) method using at least five data points with relative pressures between 0.05 and 0.30 [**40**].

NMR spectroscopy

For the liquid phase, ^{1}H NMR measurements, a Bruker Avance III DRX 300 MHz spectrometer was used. The spectra were referenced to the residual proton or carbon resonances of benzene-d6 (7.15 and 128.0 ppm) and $CDCl_3$ (7.20 and 77.0 ppm). ^{13}C CP TOSS and ^{29}Si CP solid-state NMR spectra were measured on a Bruker Avance III HD 700 MHz spectrometer with a MAS DVT 700S4 BL4 N-P/H probe. Chemical shifts were referenced externally to ^{29}Si δ [$(Me_3\text{-}SiO)_8Si_8O_{20}$]: 11.72 ppm; ^{13}C 3 [adamantane]: 38.68 ppm.

Results and discussion

Synthesis and characterization

The first step of the synthesis was a mixing of $MoO_2(acac)_2$ and H_2BPDC linker in DMF and exposure of this mixture to MW radiation similar to previously published preparation of Co-MOF and Mn-MOF materials [**42,43**]. The resulting solution of Mo-Bpdc intermediate was dropped on silicon wafer substrate followed by drying on a hot plate at 200 °C. Then, Mo-Bpdc solid product was characterized by SEM and EDX techniques (**Figs. 3S, 4S, Table 1S**). It is worth noting that SEM images show leaf-like morphology with polymeric character; the material is composed of C, O, and Mo according to EDX spectra, as expected. FTIR and Raman spectra were recorded after the product was scraped off the silicon substrate (**Fig. 5S**). Both FTIR and Raman spectra show the presence of Mo species and Bpdc linker in the Mo-Bpdc intermediate. Powder XRD pattern of dried Mo-Bpdc powder product (**Fig. 6S**) exhibits two diffractions corresponding to the diffraction lines from residual or partially reacted H_2Bpdc linker. However, besides these two diffractions Mo-Bpdc sample exhibit an amorphous character.

The synthesis continued by dropping the DMF solution of Mo-Bpdc intermediate (after MW irradiation) to APTES solution in DMF. In such a way, Mo-Bpdc-APTES microspheres were prepared via a facile approach based on the condensation reaction of Mo-Bpdc intermediate and APTES upon ethanol elimination (proved by GC-MS analysis of volatile products, **Fig. 7S**). This nonaqueous one-step reaction that produces microspheres is consid- ered a fast and straightforward method for metallosilicate preparation. In contrast to the conventional hydrolytic and impregnation methods, the preparation process is significantly facilitated and enables the incorporation of high Mo loading (see below). Finally, the Mo-Bpdc-APTES product was calcined for 3 hours at 500 °C in the air atmosphere to remove the organic linker and obtain pure inorganic porous molybdenum silicate microspheres (labeled as MoSi-500).

Powder X-Ray diffraction patterns of both Mo-Bpdc-APTES and MoSi-500 samples are given in Supplementary Information (**Fig. 8S**) and exhibit a broad profile without diffractions and indicate an

amorphous character of samples which is characteristic for silica-based materials. Notably, the MoSi-500 sample exhibits an amorphous character indicating that no phase separation of MoO_3 occurred.

Functional groups in both as-prepared Mo-Bpdc-APTES and calcined sample MoSi-500 were investigated by infrared spectroscopy. FTIR spectra are displayed in **Fig. 1** on the left. In the case of Mo-Bpdc-APTES sample, an intense absorption band raised at 1373 cm^{-1} is attributed to ν_{sym} modes of carboxylate groups [**44**]. The vibrational bands related to aromatic ring out-of-plane and C-H vibrations of the linker are found in the wavenumber region 670-790 cm^{-1} [**45**]. The vibrational bands located in regions 1527 and 1579 cm^{-1} are ascribed to ν_{asym} vibrations of carboxylate groups. The band that appeared at 1660 cm^{-1} is connected to stretching vibrations of the C=O group in DMF solvent residue [**46**]. A weak absorption band at 2928 cm^{-1} is assigned to the CH_3 stretching vibration of 3-aminopropyl group and/or residual DMF. Since a non-aqueous synthetic procedure was performed, a broad absorption band of -OH stretching vibrations has not occurred. Vibrational bands located at 1093, 1062, and 1002 cm^{-1} are characteristic of Si-O-Si/Si-O-C bonds. However, in this region, Si-O-C vibrational bands may be located as well [**47,48**]. According to the results from GC-MS analysis of reaction byproducts, it can be proposed that ethoxy groups are primarily released during the condensation of APTES with Mo-Bpdc precursor. Therefore, it is suggested that Si-O-C bonds are not present in high concentrations and vibrational bands in the region 1002-1093 cm^{-1} are most likely assigned to Si-O-Si bonds [**48**]. A vibrational band with wavenumber 962 cm^{-1} is indicative for Si-O-H/ Mo species (**Fig. 1**, on the left) [**27**]. For comparison sake, FTIR spectra of $MoO_2(Acac)_2$ and H_2Bpdc precursors are depicted in the **supplementary information** (**Fig. 9S**) as well. FTIR spectrum of calcined sample MoSi-500 shown on the left side of **Fig. 1** exhibited the most intense vibrational bands indicative of Si-O-Si bonds (1066 and 441 cm^{-1}) [**49**]. Mo-O-Si linkages are represented according to the vibrational band at 948 cm^{-1} [**15,27,50**]. It can be taken into account that no -OH vibrational bands were observed in the region around 3300-3400 cm^{-1}, indicating that Si-OH groups are not present in significant concentrations.

Prepared molybdenum silicate materials were also studied by Raman spectroscopy, as can be found in **Fig. 1** on the right. In the case of the Mo-Bpdc-APTES product, the bands with the Raman shifts 1613, 1291, 1135, and 408 cm^{-1} are attributed to the vibration modes of the Bpdc linker, while the band located at ca. 1450 cm^{-1} (labeled with an arrow) is assigned to asymmetric stretching modes of COO^- groups in MOF structure [**44**]. The MoSi-500 sample obtained from Mo-Bpdc-APTES exhibited the Raman bands at 936, 889, and 850 cm^{-1}. Further, the band located at 936 cm^{-1} is assigned to the asymmetric stretching of the highly dispersed tetrahedral di-oxo $(Si\text{-}O)_2Mo(=O)_2$ species [**51**]. Other Raman bands recorded at 889 and 850 cm^{-1} are assigned to the vibration mode of Mo=O in oligomeric species (Mo-O-Mo), which is also observed in the DRUV-Vis spectrum (see below) and to stretching mode of doubly coordinated oxygen (Mo_2-O) in threedimensional arrangement **[51-54]**. In conclusion, the Raman bands are most likely attributed to single molybdenum-oxo species or amorphous molybdenum-oxo clusters [**52,53**]. There is no evidence of MoO_3 crystal phase formation in Raman spectra **[55]**. These results are in good agreement with the amorphous character of the sample confirmed by the XRD pattern (**Fig. 8S**).

Thermogravimetric analysis was employed to investigate the thermal behavior of Mo-Bpdc-APTES sample. The analysis was performed in both atmospheres of the air and helium. TG curves are shown in **Fig. 2**.

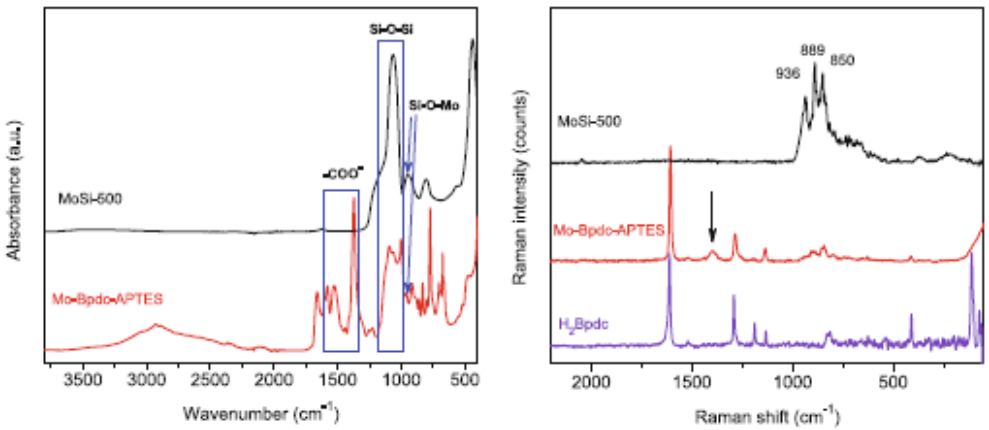

Fig. 1. Left: FTIR spectra of Mo-Bpdc-APTES and MoSi-500 products. Right: Raman spectra of Mo-Bpdc-APTES and MoSi-500 products and H_2Bpdc precursor.

A residual mass after TG analysis in the air at 1000 °C was 26.2%. There are several mass losses observed on the TG curve. The first one in the temperature range 30-175 °C (16.9%) is connected to the release of residual DMF solvent. The second mass loss (19.7%) between 175 and 350 °C is attributed to the decomposition of 3-aminopropyl groups and residual ethoxy moieties from APTES. In contrast, the last mass loss (34.7%) in the range 350-550 °C represents oxidation and decomposition of the Bpdc linker. This TG curve is shown together with a heat flow record (**Fig. 2**, red line) that reveals three exothermic effects related to the oxidation of 3-aminopropyl groups and Bpdc linker. Based on the TG curve, the temperature of 500 °C was chosen for calcination of the Mo-Bpdc-APTES material to obtain MoSi-500 catalyst subsequently. For deeper understanding and more accurate identification of released products within the heating process, a simultaneous coupled TG-FTIR analysis was performed in the atmosphere of helium. As illustrated in **Fig. 2**, the dotted line represents the TG curve recorded in helium. A 2D FTIR record displayed on the left of **Fig. 2** shows absorption bands ascribed to DMF, NH_3, and CO_2 in the ranges of 10-30, 30-60, and 60-90 minutes, respectively. Concerning TG analysis, the released products identified by FTIR analysis were connected to appropriate ranges of the TG curve (dotted line). The residual mass after TG analysis in the helium at 1000 °C is 40.1% which is about 13.9% higher than in the case of the same analysis performed in the air. This difference is due to the presence of carbon formed during the carbonization of the Bpdc linker.

Solid-state NMR spectroscopy was applied to provide information about functional groups in both as-prepared (Mo-Bpdc-APTES) and calcined (MoSi-500) samples. ^{13}C TOSS MAS NMR spectrum is depicted on the left side of **Fig. 3**. As demonstrated, the signals for different functional groups can be distinguished. The carbon atoms from the 3-aminopropyl group are found at 13.2, 24.3, and 45.0 ppm. The ethoxy group from APTES is represented by -OCH_2- with a carbon chemical shift of 60.4 ppm. The signal of the terminal carbon from an ethoxy group (reported at ca. 19 ppm) is probably overlapped by the signal from the 3-aminopropyl group [**56**]. Nevertheless, based on the intensity of signals related to ethoxy groups, it can be concluded that the content of ethoxy groups is very low. This observation confirms that ethoxy groups are mostly released in the form of ethanol (see. GC-MS **Fig. 3S**) as a

condensation byproduct produced within the reaction of APTES and Mo-Bpdc MOF species in the precursor solution. The Bpdc linker is characterized by the signals of aromatic ring carbons found in the region 125-145 ppm and by the signal of the carbonyl group at 175.7 ppm.

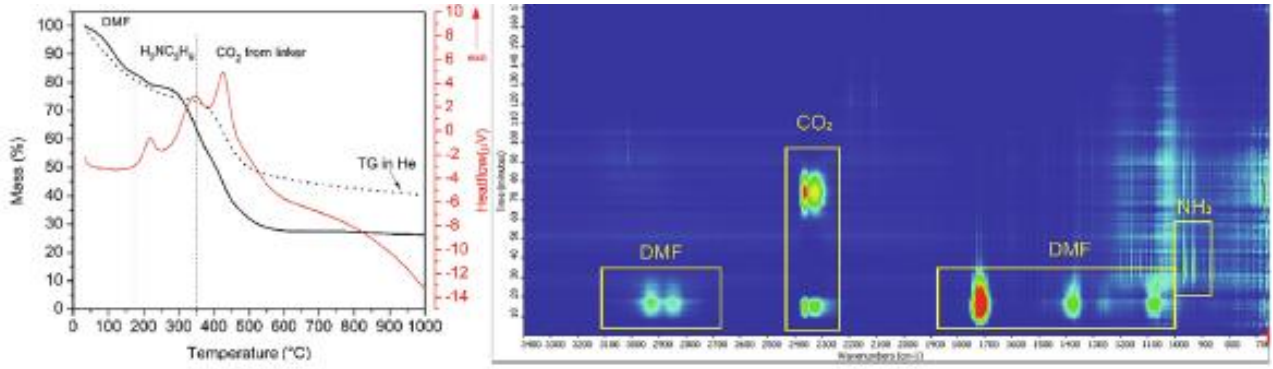

Fig. 2. Right: TG/DSC curves of Mo-Bpdc-APTES performed in the air (solid) and He (dashed) atmospheres. Left: 2D TG-FTIR map of Mo-Bpdc-APTES sample. Analysis was performed in the helium atmosphere. Spectral intensity range from blue (lowest) to red (highest).

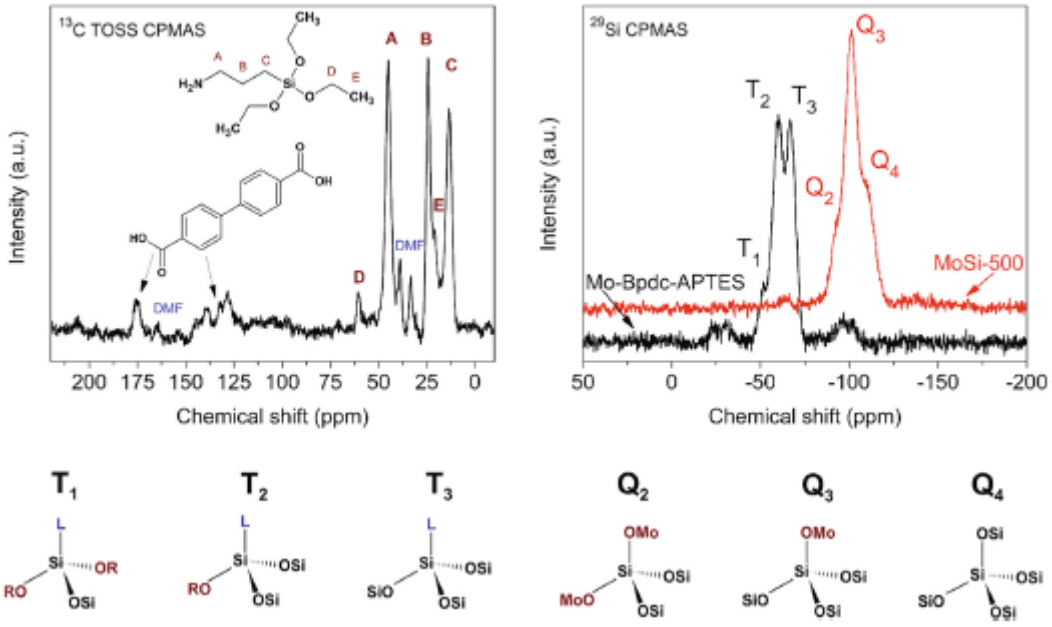

Fig. 3. Left: ^{13}C TOSS CPMAS NMR spectrum of Mo-Bpdc-APTES sample, L: 3-aminopropyl group, R: Mo, Bpdc or ethoxy group. Right: ^{29}Si CPMAS NMR spectra of Mo-Bpdc-APTES and MoSi-500 samples.

The signals with the chemical shifts 33.2, 38.8, and 164.0 ppm are assigned to DMF. ^{29}Si CPMAS NMR spectrum of Mo-Bpdc-APTES sample is shown in **Fig. 3** (on the right side). The spectrum contains three signals with the chemical shifts -51.8, -60.0, and -66.6 ppm denoted as T_1, T_2, and T_3 type groups, respectively (**Fig. 3**, bottom) [**57**]. The results obtained from the ^{29}Si CP MAS NMR spectrum of Mo-Bpdc-APTES sample confirmed the condensation of APTES and corresponds to the results from 13C TOSS CPMAS NMR (**Fig. 3**, left) and GC-MS analysis of reaction byproduct (**Fig. 3S**).

Furthermore, signals corresponding to Q_n sites in silicates were revealed in ^{29}Si CPMAS NMR spectrum of the MoSi-500 sample as displayed in **Fig. 3** on the right. This observation proved the successful transformation of organosiloxanes to fully inorganic silicates upon calcination. The most intense signal is centered at -101.1 ppm and it is assigned to Q_3 site$(MoO)Si(OSi)_3$. Besides this signal, there are shoulder peaks with the chemical shifts -110.0 and -91.9 ppm, which are attributed to Q_2 site $(MoO)_2Si(OSi)_2$ and Q_4 site $Si(OSi)_4$, respectively (**Fig. 3**, bottom) [**27,57**]. Since the FTIR method did not detect -OH groups in significant content (**Fig. 1**), it is proposed that Q_3 and Q_2 sites are most likely formed by Mo-O-Si linkages.

X-ray photoelectron spectroscopy (XPS) was employed to identify the binding relations between elements in both Mo-Bpdc-APTES and MoSi-500. Survey scans over the whole binding energy (BE) range are given in **supplementary information** (**Fig. 10S**); carbon, oxygen, silicon, nitrogen, and molybdenum peaks are identified. The XPS spectra of particular elements are depicted in **Fig. 4**. The C 1s XPS spectrum of the Mo-Bpdc-APTES sample displayed at the upper part of **Fig. 4** exhibits four signals with the binding energies 284.8, 285.4, 286.2, and 288.1 eV. The component with BE 284.8 eV is assigned to **C**-(C, H) of the aromatic rings, while the peak at 288.1 eV represents O=**C**-O species of the Bpdc linker [**42,43**]. The contribution at 286.2 eV corresponds to the **C**-O species in the residual ethoxy groups that remained after APTES con- densation. The **C**-N moieties from the 3-aminopropyl group are characterized with a component at 285.4 eV. The O 1s peak exhibited its major part at 532.1 eV. This component can be understood as oxygen in Si-O-Si bonds [**48**] formed via condensation of APTES. The contribution at the lower BE side (530.7 eV) can be ascribed to oxygen atoms coordinated to molybdenum **[28]**. The oxygen atoms from carboxylic groups of Bpdc linker are represented by a component with BE 534.0 eV. The Mo 3d XPS spectrum of Mo-Bpdc-APTES displays two distinct peaks characteristic for the doublet of $3d_{5/2}$ and $3d_{3/2}$ orbitals. The components found at binding energies 232.7 and 235.9 eV correspond to Mo(VI) $3d_{5/2}$ and Mo(VI) $3d_{3/2}$, respectively [**58**]. These values are in good agreement with the binding energies observed in the work of Jiang et al. [**59**]. Consequently, two other components found in Mo 3d spectrum at BE 231.8 and 234.9 eV are assigned to Mo(V) $3d_{5/2}$ and Mo(V) $3d_{3/2}$, respectively [**60,61**]. The Mo^{6+}/Mo^{5+} atomic concentration ratio calculated from the XPS is 1.51. The Si 2p XPS spectrum of the Mo-Bpdc-APTES sample (**Fig. 11S**) exhibits one signal centered at 102.5 eV, attributed to C-**Si**$(-O)_3$ species [**47**]. N 1s XPS spectrum depicted in the supplementary information (**Fig. 12S**) displays contributions at binding energies 399.7 and 401.5 eV characteristic for $-NH_2$ and $-NH_3^+$ species, respectively, due to the presence of the 3-aminopropyl group [**62**]. Moreover, there is also a component at 397.2 eV assigned to Mo $3p_{3/2}$.

XPS spectra of the MoSi-500 sample are illustrated in **Fig. 4** (bottom). A wide scan of the MoSi-500 sample over the whole BE region is given in **supplementary information** (**Fig. 10S**, on the right) and shows, that the intensity of the C 1s signal is much lower than that of the Mo-Bpdc-APTES sample. Based on the results of TG analysis it is assumed that carbon is released during the calcination process; thus only a small residue of carbon has remained in the sample. The carbon content in the sample determined by the XPS method is 7.1 wt%. A part of carbon amount can be present due to adventitious carbon as frequently encountered with XPS measurement. The C 1s spectrum of the MoSi-500 sample (**Fig. 13S**) contains the contributions with BE 284.8, 286.3, 287.8, and 288.7 eV attributed to **C**-(C, H), **C**-O, **C**=O, and O-**C**=O species, respectively. The O 1s spectrum exhibits two components. The major contribution at 532.7 eV is assigned to Si-**O**-Si bonds [**48**]. The latter signal with binding energy 530.8 eV corresponds to oxygen bound to molybdenum (Mo-**O**) [**28**]. In the Si 2p XPS spectrum, one signal centered at 103.4 eV was recorded. This peak is indicative of **Si**$(-O)_4$ moieties in silicate materials [**47,48**]. The Mo 3d XPS spectrum shows characteristic doublets of Mo $3d_{5/2}$ and Mo $3d_{3/2}$ orbitals. As seen in **Fig. 4** the signals with binding energies of 233.4 and 236.5 eV, are assigned to Mo(VI) $3d_{5/2}$ and Mo(VI) $3d_{3/2}$, respectively, indicating the presence of Mo^{6+} state [**63,64**]. However, there are also

contributions at BE 232.3 and 235.4 eV corresponding to Mo(V) $3d_{5/2}$ and Mo(V) $3d_{3/2}$, respectively [**60,61**]. Based on the result of XPS spectroscopy, it can be concluded that the MoSi-500 sample contains Mo^{6+} and Mo^{5+} species. The Mo^{6+}/Mo^{5+} ratio based on the XPS method is 4.1.

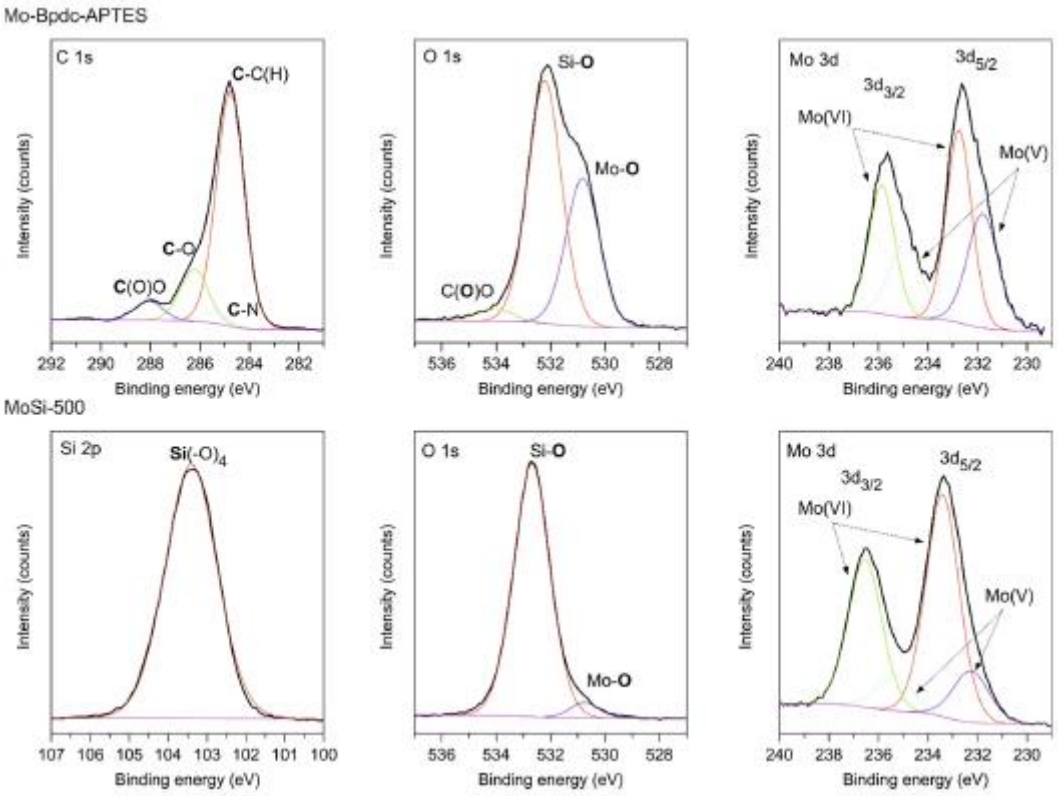

Fig. 4. XPS spectra of Mo-Bpdc-APTES (top) and MoSi-500 (bottom).

The existence of the Mo^{5+} oxidation state can be explained by the formation of oxygen vacancies in molybdenum silicate material [**61,65**]. Furthermore, the presence of Mo5+ can be ascribed to (SiO_3)-Mo=O species. Noteworthy, a presence of Mo^{5+} intermediate oxidation species was found to improve the catalytic performance of Mo-based supported catalysts for hydrodeoxygenation (HDO) of m-cresol [**66**].

The morphology of both Mo-Bpdc-APTES and MoSi-500 samples was studied by electron microscopy. SEM images of the as-prepared Mo-Bpdc-APTES sample, which are shown in **Fig. 5**-a, reveal the morphology of microspheres. The spherical morphology is also preserved in the sample MoSi-500 obtained via annealing of Mo-Bpdc-APTES at 500 °C (**Fig. 5**-b,c). As illustrated in SEM images, it can be stated that the particle size distribution is almost monodisperse. The average size of microspheres determined by SEM and TEM microscopy is about 480 nm as given in **Fig. 6**. Moreover, the particle sizes obtained from SEM and TEM images were used for the calculation of the size distribution histogram. Based on this data, the size of MoSi-500 microspheres is 479 ± 58 nm. The size distribution graphs are incorporated in **supplementary information** in **Fig. 14S**.

The homogeneity of elemental distribution is an important feature that must be considered before application in catalysis. For the investigation of elemental distribution, the STEM-EDS technique was employed. Elemental maps of the MoSi-500 sample are illustrated in **Fig. 6** at the bottom. Detailed

elemental maps of a single MoSi-500 sphere with the cross-section analyses are given in **supplementary information** (**Figs. 15S-17S**).

Based on the STEM-EDS results, it can be concluded that molybdenum species in the spheres are homogeneously distributed within the silicate matrix. This observation is crucial for following catalytic application. The elemental composition of the MoSi-500 sample was studied by EDX and STEM-EDS techniques. The surface composition was determined by the XPS method. The content (in wt%) of silicon, molybdenum, oxygen, and carbon found by different methods is listed in **Table 1**. Slight differences between the values obtained by mentioned techniques are presumably caused by carbon contamination as frequently connected with SEM and STEM. It can be emphasized that the value of molybdenum content examined by SEM-EDX (**Fig. 18S**) is in good agreement with the results obtained by ICP-OES analysis.

The Si/Mo atomic ratios determined by different methods are given in **Table 2**. As can be seen, the highest ratio (15.0) was obtained from the results of the XPS method, and it is probably caused by a slightly lower content of the molybdenum in a surface layer of MoSi-500 microspheres.

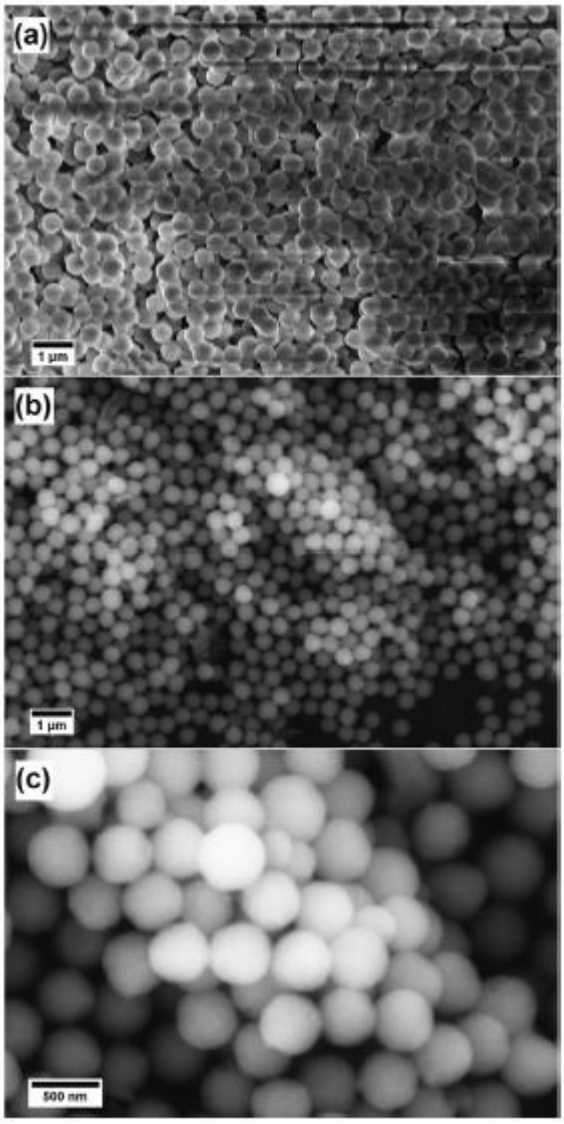

Fig. 5. SEM images of Mo-Bpdc-APTES (a) and MoSi-500 sphere samples (b, c).

On the other hand, the lowest Si/ Mo at% ratio was provided from the results of the ICP-OES analysis (7.1). However, in this case, the obtained value is close to the ratios calculated from the results of EDX and STEM-EDS analyses. Based on the at% contents determined by EDX and STEM-EDS method, the approximate formula calculated for the MoSi-500 sample can be expressed as $Mo_{0.4}Si_{3.5}O_{6.0}$. It may be pointed out that this stoichiometry is close to the stoichiometry of cage silsesquioxane (CC-POSS) or rather to the corner-opened type of silsesquioxane (IC-POSS) [**67**].

Nitrogen adsorption-desorption isotherms were measured to investigate the surface area of both Mo-Bpdc-APTES and MoSi-500 samples (**Fig. 7**). The Mo-Bpdc-APTES sample exhibited poor surface area (7 m^2 g^{-1}) based on the BET method. Nitrogen adsorp- tion/desorption isotherms of the MoSi-500 sample (**Fig. 7**) exhibit type II classification with the H4 hysteresis loop characteristic for slit-shaped pores [**68**]. The surface area is 185 m^2 g^{-1} according to the BET method with a total pore volume of 0.14 cm^3 g^{-1}. The pore diameter determined by the NLDFT method is 1.6 nm, which belongs to the microporous range.

Catalytic studies

For efficient catalytic activity, it is important to investigate the nature of the active sites in a catalyst. In the case of the MoSi-500 sample, DRUV-Vis spectroscopy and pyridine adsorption tests were performed.

In the DRUV-Vis spectrum, displayed in **Fig. 8** on the left, there are maxima at 263, 303, and 321 nm. Based on the previous investigations of different molybdenum complexes, it can be assumed that the peak at 263 nm is associated with ligand-to-metal charge transfers (LMCT) of highly dispersed tetrahedral molybdenum species (Mo^{6+}/SiO_2 (T_d) isolated dioxo-species) [**51,69,70**]. The band raised at 303 nm can be attributed to the octahedral geometry of isolated molybdenum species [**71**]. The maximum around 320 nm is due to the Mo-O-Mo bridge and is associated with molybdenum in octahedral coordination [**27,51,70,72**]. The shape of this spectral band in the region 340-400 nm could indicate the presence of both tetrahedral and octahedral molybdenum species in the silicate matrix of MoSi-500 microspheres [**27,72**].

Pyridine adsorption test was performed to investigate the surface acidity of MoSi-500 sample. The FTIR spectrum after pyridine adsorption is shown on the right side of **Fig. 8**. It unambiguously proves the presence of both Lewis and BrØnsted acid sites. As demonstrated, the vibrational band for Lewis acid sites is found at 1448 cm^{-1}, while the band at 1489 cm^{-1} indicates a combination of Lewis and BrØnsted acid sites. The Brensted acid sites are attributed to the absorption band 1540 cm^{-1} [**51**]. As it has been reported recently, the Lewis acidic sites are attributed to di-oxo $(Si\text{-}O)_2Mo(=O)_2$ species in a coordinative unsaturated tetrahedral geometry, whereas the Brensted acidity is proposed to be a consequence of the interaction between silanol groups and adjacent surface species under formation of pseudo-bridging Si—O(H)—Mo $(=O)_2$ species [**8**].

Further, the catalytic activity of MoSi-500 spheres was tested in two model reactions. The first one was epoxidation of cyclohexene to cyclohexene oxide (**Fig. 19S**). The reaction was performed according to published procedures [**10,36**] in toluene at 65 °C with 20 mg of catalyst. The blank reaction without the MoSi-500 catalyst was conducted under the same conditions; no products were observed after two hours. Catalytic conversions were evaluated by ^1H NMR spectroscopy (based on cyclohexene) and/or GC-MS spectrometry (based on cumyl hydroperoxide; **Fig. 20S, 21S**; **Table 2S**) for the sake of comparison. The results taken from different runs and analyzed by the two respective methods showed only minor differences (**Table 3**). These results confirm that cumyl hydroperoxide reacted

effectively and did not suffer from ineffective decomposition. ^{1}H NMR results were used for the evaluation of the TOF value. As displayed in Table 3, the catalytic conversions of cyclohexene after two hours determined by ^{1}H NMR and GC-MS were 84 and 86%, respectively, with the 90% selectivity to cyclohexene oxide (r.t. 2.2 min. in GC chromatogram). Cyclohexanol and cyclohexanone were detected in GC chromatogram as minor products with the selectivity of 9 and 1%, respectively. The conversion percentage was also studied in dependence on the reaction time (**Fig. 22S**). After 4 and 6 hours, the conversion determined by GC-MS reached 90% and 96%, respectively. The results are listed in **Table 3** and illustrated in **Fig. 9**. The comparison of curves reflecting catalytic activity in time obtained from the results determined by ^{1}H NMR and GC-MS is depicted in **Fig. 9**. As shown, the curves exhibited almost the same shape, and the results are in good agreement.

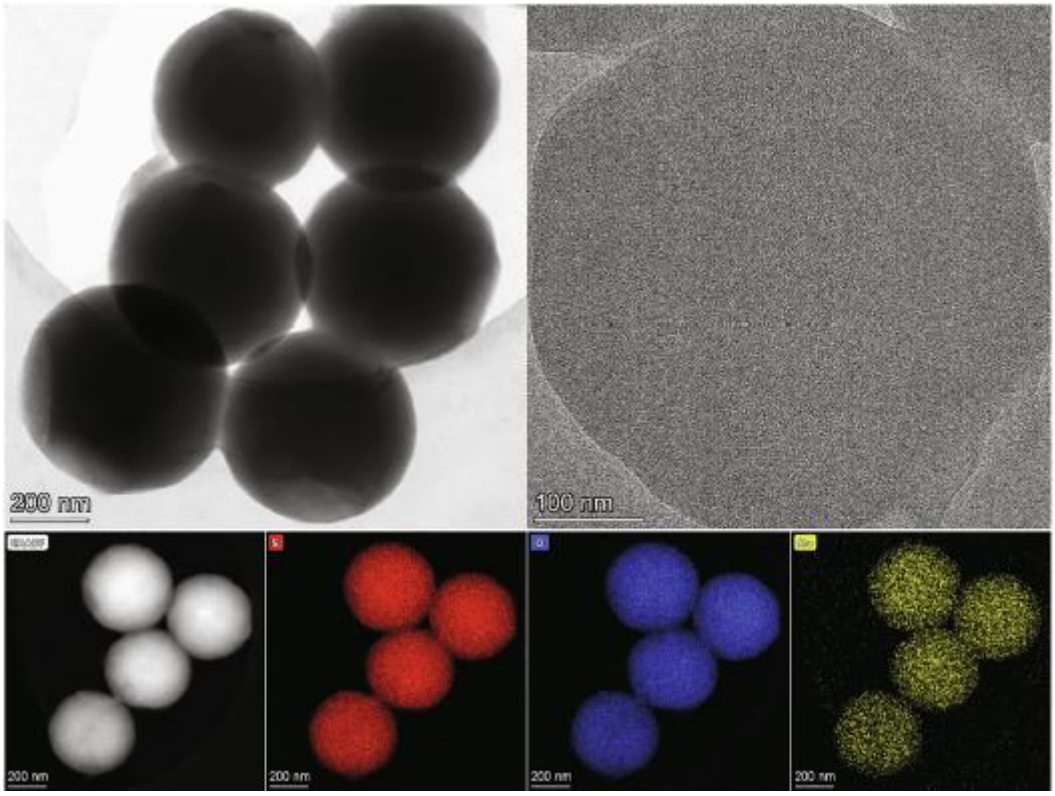

Fig. 6. TEM images of MoSi-500 spheres (upper). At the bottom: STEM-EDS elemental maps of MoSi-500 spheres sample (red - Si, blue - O, yellow - Mo).

Table 1 Elemental composition of MoSi-500 sample determined by different methods.

Method	wt %		
	Si	Mo	O
EDX	37.67	15.56	43.22
STEM-EDS	43.32	16.95	39.73
XPS	43.49	9.9	39.48
ICP-OES	31.4	15.2	–

Table 2 The Si/Mo atomic ratios determined by different methods.

at% ratio	EDX	STEM-EDS	XPS	ICP
Si/Mo	8.2	8.7	15.0	7.1

It should be stressed out that the TOF number, which is an important value of catalyst performance characterization, is given in **Table 4** [**37**].

The leaching test was performed as follows: MoSi-500 catalyst had been heated in toluene under reflux for 4 hours. Then, the catalyst was separated, and the solution was used for catalytic epox-idation of cyclohexene performed at 65 °C for 2 h. The reaction efficiency was evaluated by GC-MS chromatography. The chromatograms after catalytic reaction, blank reaction, and after leaching test are shown on the left side of **Fig. 10**. As can be seen, the GC chromatogram of blank and leaching test reactions are similar. It has to be pointed out that no catalytic reaction runs without the catalyst which was achieved after the leaching test.

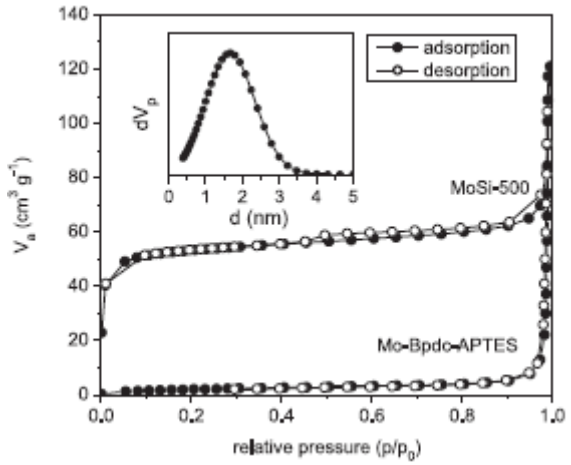

Fig. 7. Nitrogen adsorption/desorption isotherms of Mo-Bpdc-APTES and MoSi-500 samples. Inset: Pore size distribution determined by NLDFT method (adsorption range).

In other words, no active sites from the MoSi-500 catalyst are released into the solution, and the nature of the catalytic reaction is exclusively heterogeneous.

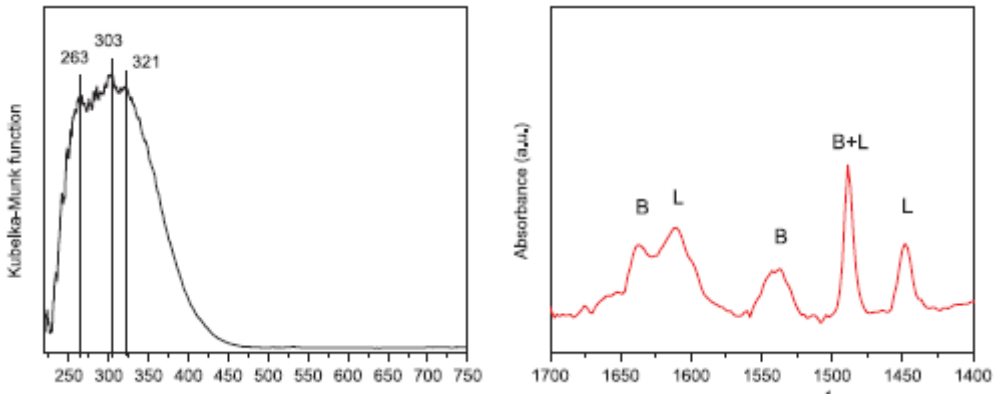

Fig. 8. Left: DRUV-Vis spectrum of MoSi-500 catalyst. Right: FTIR spectrum of MoSi-500 catalyst after pyridine adsorption (L: Lewis, B: Bransted).

Table 3 MoSi-500 catalyst performance in epoxidation of cyclohexene.

Catalyst/time	conversion [%] ^{1}H NMR [a]/GC–MS [b]						selectivity [c]
	10	30	60	120	240	360	I/II/III
MoSi-500	30/28	57/59	71/76	84/86	91/90	>99/96	90:9:1

[a] *based on ^{1}H NMR spectra integration (signals of cyclohexene and cyclohexene oxide).*

[b] *based on the ratio of integral intensities of cyclohexene oxide and cumyl hydroperoxide.*

[c] *I - cyclohexene oxide, II - cyclohexanol, III - cyclohexanone.*

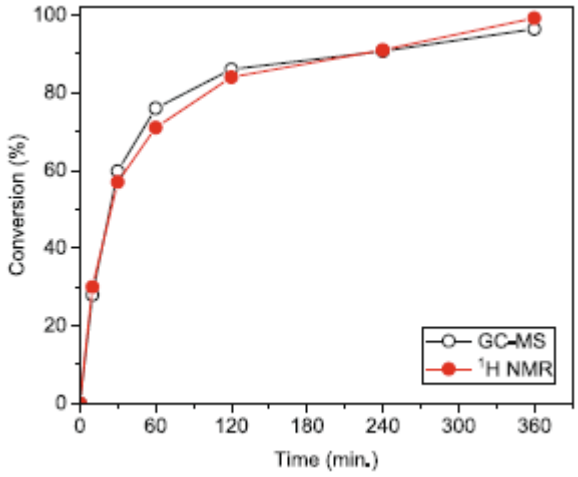

Fig. 9. The curve of cyclohexene conversion in time (determined by ^{1}H NMR spectroscopy and GC-MS spectrometry).

The reusability of the MoSi-500 catalyst was studied after the separation of catalyst and drying at 150 °C. The products of the catalysis were analysed after 2 hours and it is shown that conversion decreased within the second and third cycles (**Fig. 10** on the right).

Table 4 Characterization of MoSi-500 catalyst and TOF number.

Catalyst	Mo content (ICP) [wt%]	Weight of catalyst [mg]	Mo content in the catalyst		TOF [h^{-1}][a]
			[mg]	[mmol]	
MoSi-500	15.2	20	3.04	0.031	285

[a] *after 10 min of catalytic reaction.*

This issue can be caused by the low temperature of catalyst reactivation or by the presence of residual organic substrates, which can occupy active molybdenum sites. After three cycles, the MoSi-500 catalyst was calcined at 400 °C, and its catalytic activity and selectivity to cyclohexene in the following fourth cycle significantly recovered. The cyclohexene conversion in the fourth cycle reached 78% with the 95% selectivity to cyclohexene oxide. These results confirm the reusability of the MoSi-500 catalyst. The MoSi-500 catalyst's performance was compared with the results obtained by other reported molybdenum-silica catalysts for cyclohexene epoxidation. The comparison is given in **Table 5**. It has to be pointed out that in the case of the presented MoSi-500 catalyst, the high conversion of cyclohexene at moderate temperature and even in the short reaction time was achieved. Moreover, in our case, the weight of the catalyst compared to others is reduced. This was achieved thanks to a peculiar non-aqueous synthetic approach that allowed the introduction of a much higher amount of active

molybdenum species into the silica network in comparison to other catalysts, as can be found in **Table 5**, and at the same time to maintain the high homogeneity of atom mixing.

The morphology of the used catalyst after the 4th cycle was investigated by powder X-Ray diffraction (PXRD) and SEM-EDX technique. As demonstrated in PXRD patterns (**Fig. 23S**), both the used and fresh catalysts exhibited amorphous character, and no diffraction patterns indicating MoO_3 crystalline phase were observed. As can be seen in **Fig. 23S**, the SEM image of the used catalyst confirms that spherical morphology has been preserved. The elemental composition and particularly the content of silicon and molybdenum in the used MoSi-500 catalyst has remained almost unchanged and very similar to the composition of the fresh MoSi-500 catalyst determined by EDX method (**Fig. 24S; Table 3S**).

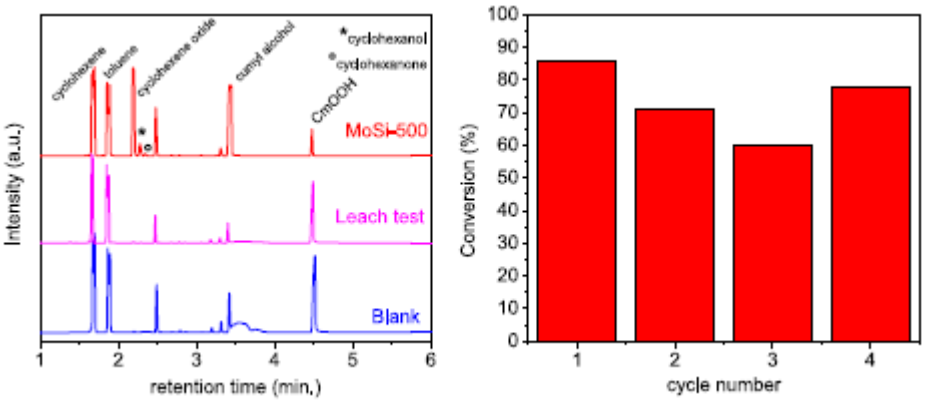

Fig. 10. Left: A comparison of GC chromatograms after catalytic epoxidation reaction with blank reaction and catalytic reaction after leaching test. Reaction condition: 20 mg of catalyst, 5 cm^3 of toluene, 24.7 mmol of cyclohexene, 4.9 mmol CmOOH, reaction temperature and time: 65 °C and 2 h, respectively. Right: The conversions achieved with recycled catalysts (after the 3rd cycle, the catalyst was heated at 400 °C).

Table 5 The comparison of various molybdenum-silica-based catalysts for cyclohexene epoxidation.

Catalyst	Mo content [wt%]	m catalyst [mg]	temperature [°C]	time [h]	conversion [%]	TOF [h^{-1}]	Ref.
MoOx@HSS-2	3	75	80	8	67	4	[9]
MoO2phenalaacacAmpMCM-41	0.49	100	62	9	87	255	[26]
Mo/HMSS-X	0.23	25	80	4	85	893	[15]
Mo-TUD-1	5	100	40	6	35	25	[73]
Mo-MCM41	2.5	100	80	4	93	179	[74]
MoO3@SiO2-400-1/2	3.39	25	70	4	65	46	[29]
MoO3@3D-DMSNs-5	6.99	25	70	6	58	7	[31]
MoSi-500	15.2	20	65	2	86	285 [a]	this work

*TOF: mmol of reactant consumed/(mmol of Mo in catalyst * time).*

[a] *after 10 min of catalytic reaction.*

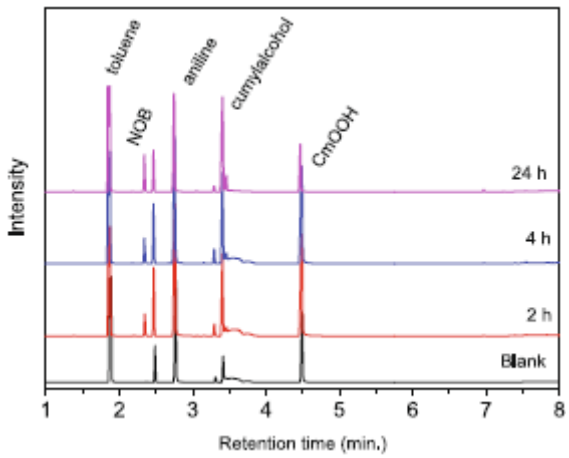

Fig. 11. GC chromatograms of the reaction mixture after catalytic aniline oxidation reaction.

Table 6 Conversion of aniline to nitrosobenzene in the presence of MoSi-500 catalyst.

Time [h]	2	4	24
Conversion [%]	8	9	14

Furthermore, the catalytic oxidation of aniline with cumene hydroperoxide in the presence of MoSi-500 catalyst was performed. The nitroso- compounds are conventionally prepared via the methods using peracids **[6]**. Moreover, the oxidation of aniline usually leads to azo- and azoxy- derivatives that decrease a selectivity to nitroso- compounds. It has already been reported that molybdenum compounds can catalyze aniline oxidation with high selectivity to nitroso- compounds **[4]**. The catalytic reaction presented here was conducted with 20 mg of MoSi-500 catalyst at room temperature. The GC-MS chromatograms of catalytic reaction mixtures show a clear peak corresponding to nitrosobenzene (NOB), while blank reaction without the catalyst displayed no oxidation product (**Fig. 11**).

The conversions determined by the GC-MS technique are given in **Table 6**. As can be observed, the conversion numbers are not as high as in the case of epoxidation reactions. However, the MoSi-500 catalyst is significantly active in aniline oxidation at room temperature with high selectivity (>99%) to NOB. Only a trace of azobenzene (<0.5%) was detected in the chromatogram (r.t. 6.98 min) after 24 h.

To compare the catalytic activity of MoSi-500 with other Mo-based catalysts for aniline oxidation, molybdenum acetylide oxo-peroxo complex can be considered **[4]**. This catalyst with 30% hydrogen peroxide as an oxidant achieved a conversion of 97% after a 12 h reaction at room temperature. However, in this case, due to the organometallic structure of the catalyst, the possibility of homogeneous catalysis may be considered. The organometallic coordination polymer [(n-$Bu_3Sn)_2MoO_4$] reported by Bordoloi et al. achieved 77% conversion of aniline to NOB [**75**]. However, it should be noted that the molar ratio of aniline to [(n-$Bu_3Sn)_2MoO_4$] catalyst is 10 while the molar ratio of aniline to molybdenum contained in 20 mg of MoSi-500 catalyst is ca. 158. Recently, Han et al. have described molecular molybdenum oxide catalyst for selective oxidation of aniline, but in this case, the aniline oxidation led to azobenzenes and azoxybenzenes [**76**]. Oxidation of aniline over MoO_3 with the addition of KOH base and H_2O_2 as oxidant has been reported by Defoin [**5**]. The conversion of aniline

to NOB after 24 h reached 65%. It should be pointed out that without the base added, the conversion after one day reached 15%. For example, in the comparison to the commercial CeO_2 catalyst, which shows conversion of 10% after 12 hours [**77**], the presented MoSi-500 catalyst achieves a conversion of 9% and 14% after 4 and 24 hours, respectively. Moreover, in the case of commercial CeO_2, the selectivity to NOB is lower than that observed for the MoSi-500 catalyst. It can be argued that the MoSi-500 catalyst has exhibited better performance for selective oxidation of aniline to NOB than commercial CeO_2 nanoparticles.

Conclusion

In this work, a novel preparation method for molybdenum silicate microspheres is presented. The synthesis involves a microwave-assisted preparation of Mo-Bpdc MOF-based precursor and its subsequent condensation with 3-aminopropyltriethoxysilane under non-aqueous conditions. The formation of monodisperse molybdenum silicate microspheres was observed. The Mo-Bpdc-APTES product was calcined at 500 °C to remove the linker and residual functional groups. As a result, the calcined product MoSi-500 exhibited amorphous and porous character and homogeneous distribution of molybdenum species. It is worth mentioning that the preparation method reported here provides a product with a relatively high molybdenum content but without its phase separation in the form of MoO_3. MoSi-500 spheres were used as heterogeneous catalysts for the epoxidation of cyclohexene and oxidation of aniline. It was found that the catalyst exhibited high efficiency in the epoxi-dation reaction with the conversion of 86% after 2 h with the 90% selectivity to cyclohexene oxide and TOF about 285 h^{-1}. The reusability of catalyst was studied within four cycles, and the conversion after the fourth cycle was 78% with the 95% selectivity to cyclohexene oxide. Furthermore, it was proved that no leaching of active sites occurs; thus, the presented catalyst is truly heterogeneous. The catalytic oxidation of aniline at room temperature yielded the conversion of 14% after 24 h with the selectivity >99% to nitrosobenzene. Therefore, the significant selective catalytic activity of MoSi-500 spheres for aniline oxidation was confirmed. In summary, the non-aqueous preparation method reported here provides homogeneous molybdenum silicate microspheres in one step without the need to prepare the silicate support in a separate step. Moreover, it was demonstrated that the described approach enables obtaining an efficient heterogeneous oxidation catalyst, which makes it a promising candidate with a potential application at the industrial level.

References

[1] J.C. Védrine, ChemSusChem 12 (3) (2019) 577-588, **https://doi.org/10.1002/ cssc.201802248**.

[2] W. Yan, M. Liu, J. Wang, J. Shen, S. Zhang, X. Xu, S. Wang, J. Ding, X. Jin, Chem. Rec. 20 (3) (2020) 230-251, **https://doi.org/10.1002/tcr.201900037**.

[3] R.A. Setien, S. Ghasemi, G. Pourhashem, D.C. Webster, Polym. Int. 70 (5) (2021) 594-603, **https://doi.org/10.1002/pi.6193**.

[4] A.V. Biradar, T.V. Kotbagi, M.K. Dongare, S.B. Umbarkar, Tetrahedron Lett. 49 (22) (2008) 3616-3619, **https://doi.org/10.1016Zj.tetlet.2008.04.005**.

[5] A. Defoin, Synthesis (Stuttg). 2004 (05) (2004) 706-710, **https://doi.org/ 10.1055/s-2004-815964**.

[6] B.G. Gowenlock, G.B. Richter-Addo, Chem. Rev. 104 (7) (2004) 3315-3340, **https://doi.org/10.1021/cr030450k**.

[7] V. Smeets, E.M. Gaigneaux, D.P. Debecker, ChemCatChem (2021) 1-26, **https:// doi.org/10.1002/cctc.202101132**.

[8] K. Amakawa, Y. Wang, J. Krohnert, R. Schlogl, A. Trunschke, Mol. Catal. 478 (April) (2019), **https://doi.org/10.1016/j.mcat.2019.110580**.

[9] Y. Kuwahara, N. Furuichi, H. Seki, H. Yamashita,J. Mater. Chem. A5(35) (2017) 18518-18526, **https://doi.org/10.1039/C7TA06288E**.

[10] V. Lafond, P.H. Mutin, A. Vioux, J. Mol. Catal. A Chem. 182-183 (2002) 81-88, **https://doi.org/10.1016/S1381-1169(01)00487-3**.

[11] M.S. Holzwarth, B. Plietker, ChemCatChem 5 (7) (2013) 1650-1679, **https:// doi.org/10.1002/cctc.201200592**.

[12] J. Morlot, N. Uyttebroeck, D. Agustin, R. Poli, ChemCatChem 5 (2) (2013) 601611, **https://doi.org/10.1002/cctc.201200068**.

[13] S. Lwin, I.E. Wachs, ACS Catal. 4 (8) (2014) 2505-2520, **https://doi.org/ 10.1021/cs500528h**.

[14] K. Ding, A. Gulec, A.M. Johnson, T.L. Drake, W. Wu, Y. Lin, E. Weitz, L.D. Marks, P.C. Stair, ACS Catal. 6 (9) (2016) 5740-5746, **https://doi.org/10.1021/ acscatal.6b00098**.

[15] Y. Shen, P. Jiang, J. Zhang, G. Bian, P. Zhang, Y. Dong, W. Zhang, Mol. Catal. 433 (2017) 212-223, **https://doi.org/10.1016/j.mcat.2016.12.011**.

[16] D.P. Debecker, K. Bouchmella, M. Stoyanova, U. Rodemerck, E.M. Gaigneaux, P. Hubert Mutin, Catal. Sci. Technol. 2(6) (2012) 1157. 10.1039/c2cy00475e.

[17] A. Saraeian, S.J. Burkhow, D. Jing, E.A. Smith, B.H. Shanks, A.C.S. Sustain, Chem. Eng. 9 (19) (2021) 6685-6696, **https://doi.org/10.1021/acssuschemeng.1c00295**.

[18] S. Liu, X. Li, W. Xin, S. Xie, P. Zeng, L. Zhang, L. Xu, J. Nat. Gas Chem. 19 (5) (2010) 482-486, **https://doi.org/10.1016/S1003-9953(09)60095-5**.

[19] K. Tao, Q. Ma, N. Tsubaki, S. Zhou, L. Han, Catal, . A Chem. 416 (2016) 39-46, **https://doi.org/10.1016/j.molcata.2016.02.019**.

[20] A. Zarnegaryan, S. Kargar, Appl. Surf. Sci. Adv. 4(November 2020) (2021) 100073. 10.1016/j.apsadv.2021.100073.

[21] D.P. Debecker, M. Stoyanova, U. Rodemerck, A. Léonard, B.-L. Su, E.M. Gaigneaux, Catal, . Today 169 (1) (2011) 60-68, **https://doi.org/10.1016/ j.cattod.2010.07.026**.

[22] D.P. Debecker, M. Stoyanova, U. Rodemerck, E.M. Gaigneaux, 2010, pp. 581-5.

[23] R. Neumann, M. Levin-Elad, J. Catal. 166 (2) (1997) 206-217, **https://doi.org/ 10.1006/jcat.1997.1479**.

[24] D.P. Debecker, M. Stoyanova, U. Rodemerck, E.M. Gaigneaux, J. Mol. Catal. A Chem. 340(1-2) (2011)65-76, **https://doi.org/10.1016/j.molcata.2011.03.011**.

[25] U. Arnold, R. Serpa da Cruz, D. Mandelli, U. Schuchardt, J. Mol. Catal. A Chem. 165 (1-2) (2001) 149-158, **https://doi.org/10.1016/S1381-1169(00)00408-8**.

[26] M. Masteri-Farahani, J. Mol. Catal. A Chem. 316 (1-2) (2010) 45-51, **https://doi.org/10.1016/j.molcata.2009.09.020**.

[27] F. Adam, A. Iqbal, Microporous Mesoporous Mater. 141 (1-3) (2011) 119-127, **https://doi.org/10.1016/j.micromeso.2010.10.037**.

[28] J. Wang, X. Li, S. Zhang, R. Lu, Nanoscale 5 (11) (2013) 4823, **https://doi.org/10.1039/c3nr01097j**.

[29] Y. Shen, P. Jiang, Y. Wang, G. Bian, P.T. Wai, Y. Dong, J. Solid State Chem. 264 (April) (2018) 156-164, **https://doi.org/10.1016/jjssc.2018.05.005**.

[30] Y. Shen, P. Jiang, L. Wang, G. Bian, P.T. Wai, P. Zhang, Y. Dong, ChemistrySelect 3 (31) (2018) 9084-9090, **https://doi.org/10.1002/slct.201801955**.

[31] Q. Gu, P. Jiang, Y. Shen, K. Zhang, P.T. Wai, A. Haryono, J. Porous Mater. 28 (3) (2021) 779-789, **https://doi.org/10.1007/s10934-021-01031-1**.

[32] J. Zhang, Y. Zhao, A. Li, H. Ye, Q. Shang, X. Shi, Y. Shen, J. Porous Mater. 26 (3) (2019) 869-880, **https://doi.org/10.1007/s10934-018-0684-2**.

[33] D. Skoda, A. Styskalik, Z. Moravec, P. Bezdicka, M. Babiak, M. Klementova, C.E. Barnes, J. Pinkas, RSC Adv. 6(29) (2016) 24273-84. 10.1039/C5RA24563J.

[34] D. Skoda, A. Styskalik, Z. Moravec, P. Bezdicka, J. Pinkas, J. Mater. Sci. 50 (9) (2015) 3371-3382, **https://doi.org/10.1007/s10853-015-8888-1**.

[35] A. Styskalik, D. Skoda, C. Barnes, J. Pinkas, Catalysts 7 (6) (2017) 168, **https://doi.org/10.3390/catal7060168**.

[36] D. Skoda, A. Styskalik, Z. Moravec, P. Bezdicka, C.E. Barnes, J. Pinkas, J. Sol-Gel Sci. Technol. 74 (3) (2015) 810-822, **https://doi.org/10.1007/s10971-015-3666-8**.

[37] S. Kozuch, J.M.L. Martin, ACS Catal. 2 (12) (2012) 2787-2794, **https://doi.org/10.1021/cs3005264**.

[38] F. Schuth, M.D. Ward, J.M. Buriak, Chem. Mater. 30 (11) (2018) 3599-3600, **https://doi.org/10.1021/acs.chemmater.8b01831**.

[39] M. Jacquemin, M.J. Genet, E.M. Gaigneaux, D.P. Debecker, ChemPhysChem 14 (15) (2013) 3618-3626, **https://doi.org/10.1002/cphc.201300411**.

[40] S. Lowell, J.E. Shields, M.A. Thomas, M. Thommes, Characterization of Porous Solids and Powders: Surface Area, Pore Size and Density, Springer, Netherlands, 2004, pp. 58-81.

[41] J. Rouquerol, F. Rouquerol, P. Llewellyn, G. Maurin, K. Sing, Adsorption by Powders and Porous Solids Principles, Methodology and Applications, Academic PressAmsterdam, 2014.

[42] D. Skoda, T. Kazda, L. Munster, B. Hanulikova, A. Styskalik, P. Eloy, D.P. Debecker, P. Vyroubal, L. Simonikova, I. Kuritka, J. Mater. Sci. 54(22) (2019) 14102-22. 10.1007/s10853-019-03871-4.

[43] D. Skoda, T. Kazda, L. Munster, B. Hanulikova, A. Styskalik, P. Eloy, D.P. Debecker, J. Vilcakova, O. Cech, L. Simonikova, V. Kanicky, I. Kuritka, J. Energy Storage 27 (2020) 101113.

[44] N.R. Dhumal, M.P. Singh, J.A. Anderson, J. Kiefer, H.J. Kim, J. Phys. Chem. C 120 (6) (2016) 3295-3304, **https://doi.org/10.1021/acs.jpcc.5b10123**.

[45] L. Valenzano, B. Civalleri, S. Chavan, S. Bordiga, M.H. Nilsen, S. Jakobsen, K.P. Lillerud, C. Lamberti, Chem. Mater. 23(7) (2011) 1700-18. 10.1021/ cm1022882.

[46] A. Shastri, A.K. Das, S. Krishnakumar, P.J. Singh, B.N. Raja Sekhar, J. Chem. Phys. 147 (22) (2017), **https://doi.org/10.1063/1.5006126**.

[47] E. Lecoq, D. Duday, S. Bulou, G. Frache, F. Hilt, R. Maurau, P. Choquet, Plasma Process. Polym. 10 (3) (2013) 250-261, **https://doi.org/10.1002/ppap.201200108**.

[48] P. Post, L. Wurlitzer, W. Maus-Friedrichs, A. Weber, Nanomaterials 8 (7) (2018) 530, **https://doi.org/10.3390/nano8070530**.

[49] Y. Huang, Z. Jiang, W. Schwieger, Chem. Mater. 11 (5) (1999) 1210-1217, **https://doi.org/10.1021/cm980403m**.

[50] T. Ono, M. Anpo, Y. Kubokawa, J. Phys. Chem. 90 (20) (1986) 4780-4784, **https://doi.org/10.1021/j100411a014**.

[51] A. Uchagawkar, A. Ramanathan, Y. Hu, B. Subramaniam, Catal. Today 343 (2019) (2020) 215-25. 10.1016/j.cattod.2019.03.073.

[52] L. Gong, S.C. Haur, J. Mater. Chem. C 5 (8) (2017) 2090-2097, **https://doi.org/ 10.1039/C6TC04580D**.

[53] K. Ajito, L.A. Nagahara, D.A. Tryk, K. Hashimoto, A. Fujishima, J. Phys. Chem. 99 (44) (1995) 16383-16388, **https://doi.org/10.1021/j100044a028**.

[54] C.E. Ciocan, E. Dumitriu, T. Cacciaguerra, F. Fajula, V. Hulea, Catal. Today 198 (1) (2012) 239-245, **https://doi.org/10.1016/j.cattod.2012.04.071**.

[55] M. Dieterle, G. Weinberg, G. Mestl, Phys. Chem. Chem. Phys. 4 (5) (2002) 812821, **https://doi.org/10.1039/b107012f**.

[56] T. Gutmann, A. Grunberg, N. Rothermel, M. Werner, M. Srour, S. Abdulhussain, S. Tan, Y. Xu, H. Breitzke, G. Buntkowsky, Solid State Nucl. Magn. Reson. 55-56 (2013) 1-11. 10.1016/j.ssnmr.2013.06.004.

[57] I.S. Protsak, Y.M. Morozov, W. Dong, Z. Le, D. Zhang, I.M. Henderson, Nanoscale Res. Lett. 14 (1) (2019) 160, **https://doi.org/10.1186/s11671-019-2982-2**.

[58] J. Baltrusaitis, B. Mendoza-Sanchez, V. Fernandez, R. Veenstra, N. Dukstiene, A. Roberts, N. Fairley, Appl. Surf. Sci. 326 (2015) 151-61. 10.1016/j. apsusc.2014.11.077.

[59] H. Jiang, R. Lu, X. Si, X. Luo, J. Xu, F. Lu, ChemCatChem 11 (17) (2019) 42914296, **https://doi.org/10.1002/cctc.201900332**.

[60] W.J. Dong, J. Ham, G.H. Jung, J.H. Son, J.-L. Lee, J. Mater. Chem. A4 (13) (2016) 4755-4762, **https://doi.org/10.1039/C5TA10032A**.

[61] M. Rellán-Pineiro, N. López, J. Phys. Chem. Lett. 9 (10) (2018) 2568-2573, **https://doi.org/10.1021/acs.jpclett.8b00536**.

[62] J. Ederer, P. Janoš, P. Ecorchard, J. Tolasz, V. Štengl, H. Beneš, M. Perchacz, O. Pop-Georgievski, RSC Adv. 7(21) (2017) 12464-73. 10.1039/C6RA28745J.

[63] S. Xie, D. Cao, Y. She, H. Wang, J.-W. Shi, M.K.H. Leung, C. Niu, Chem. Commun. 54 (56) (2018) 7782-7785, **https://doi.org/10.1039/C8CC04282A**.

[64] A. Ramanathan, J.F. Wu, R. Maheswari, Y. Hu, B. Subramaniam, Microporous Mesoporous Mater. 245 (2017) 118-125, **https://doi.org/10.1016/j.micromeso.2017.03.001**.

[65] S. Shen, X. Zhang, X. Cheng, Y. Xu, S. Gao, H. Zhao, X. Zhou, L. Huo, ACS Appl. Nano Mater. 2 (12)(2019) 8016-8026, **https://doi.org/10.1021/acsanm.9b02072**.

[66] M. Shetty, K. Murugappan, T. Prasomsri, W.H. Green, Y. Román-Leshkov, J. Catal. 331 (2015) 86-97, **https://doi.org/10.1016/j.jcat.2015.07.034**.

[67] H. Imoto, Y. Ueda, Y. Sato, M. Nakamura, K. Mitamura, S. Watase, K. Naka, Eur. J. Inorg. Chem. 2020 (9) (2020) 737-742, https://doi.org/10.1002/ ejic.201901182.

[68] M. Thommes, Chem. Ing. Technol. 82 (7) (2010) 1059-1073, **https://doi.org/ 10.1002/cite.201000064**.

[69] R. Santalucia, G. Spoto, L. Mino, Molecules 26 (6) (2021) 1700, **https://doi.org/ 10.3390/molecules26061700**.

[70] C. Lin, K. Tao, H. Yu, D. Hua, S. Zhou, Catal. Sci. Technol. 4 (11) (2014) 40104019, **https://doi.org/10.1039/C4CY00652F**.

[71] J.P. Thielemann, T. Ressler, A. Walter, G. Tzolova-Muller, C. Hess, Appl. Catal. A Gen. 399 (1-2) (2011) 28-34, **https://doi.org/10.1016Zj.apcata.2011.03.032**.

[72] A. Duan, G. Wan, Z. Zhao, C. Xu, Y. Zheng, Y. Zhang, T. Dou, X. Bao, K. Chung, Catal. Today 119 (1-4) (2007) 13-18, **https://doi.org/10.1016/j.cattod.2006.08.049**.

[73] M.S. Hamdy, G. Mul, Catal. Sci. Technol. 2 (9) (2012) 1894-1900, **https://doi. org/10.1039/c2cy20073b**.

[74] F. Bigi, C.G. Piscopo, G. Predieri, G. Sartori, R. Scotti, R. Zanoni, R. Maggi, J. Mol. Catal. A Chem. 386 (2014) 108-113, **https://doi.org/10.1016/j.molcata.2014.01.028**.

[75] A. Bordoloi, S.B. Halligudi, Adv. Synth. Catal. 349 (13) (2007) 2085-2088, **https://doi.org/10.1002/adsc.200700224**.

[76] S. Han, Y. Cheng, S. Liu, C. Tao, A. Wang, W. Wei, H. Yu, Y. Wei, Angew. Chem. 133 (12) (2021) 6452-6455, **https://doi.org/10.1002/ange.202013940**.

[77] B. Paul, S.K. Sharma, S. Adak, R. Khatun, G. Singh, D. Das, V. Joshi, S. Bhandari, S. S. Dhar, R. Bal, New J. Chem. 43(23) (2019) 8911-8. 10.1039/C9NJ01085H.